

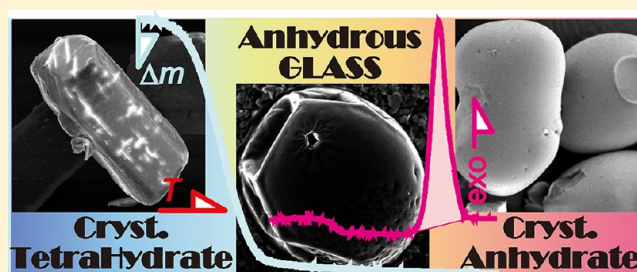
Thermal Dehydration of Magnesium Acetate Tetrahydrate: Formation and in Situ Crystallization of Anhydrous Glass

Nobuyoshi Koga,* Yasumichi Suzuki, and Tomoyuki Tatsuoka

Chemistry Laboratory, Department of Science Education, Graduate School of Education, Hiroshima University, 1-1-1 Kagamiyama 739-8524, Japan

S Supporting Information

ABSTRACT: The kinetics and mechanism of the thermal dehydration of magnesium acetate tetrahydrate were investigated as a typical example of the glass formation process via the thermal decomposition of solids. Formation of an intermediate fluid phase was identified as the characteristic phenomenon responsible for the formation of anhydrous glass. Thermal dehydration from the surface fluid layer regulates the zero-order-like rate behavior of the mass-loss process with an apparent activation energy $E_a \approx 70\text{--}80\text{ kJ mol}^{-1}$. Because of variations in the mechanism of release of the water vapor with changes in the reaction temperature range, the mass-loss behavior is largely dependent on the particle size of the sample and heating conditions. The formation of hollow anhydrous glass is the novel finding of the present study. The mechanism of formation is discussed in terms of complementary interpretations of the morphological changes and kinetic behavior of the thermal dehydration. On further heating, the as-produced anhydrous glass exhibits a glass transition phenomenon at approximately 470 K with an $E_a \approx 550\text{--}560\text{ kJ mol}^{-1}$, and subsequently crystallizes via the three-dimensional growth of nuclei controlled by diffusion. The crystallization process is characterized by an $E_a \approx 280\text{ kJ mol}^{-1}$ and an enthalpy change $\Delta H = -13.3\text{ kJ mol}^{-1}$, resulting in the formation of smaller, rounded particles of crystalline anhydrate.



1. INTRODUCTION

In many technical processes used for material synthesis, thermal decomposition reactions of solids that produce noncrystalline materials are encountered, but the mechanisms and kinetic characteristics of such processes have not as yet been fully revealed.^{1,2} In the thermal dehydration of some crystalline hydrates, a noncrystalline anhydrate is produced via an intermediate fluid phase, indicating thermal behavior similar to that observed in the sol–gel process associated with glass formation.^{3–8} The thermal dehydration of magnesium acetate tetrahydrate is known as a process which produces noncrystalline anhydrate.^{9–11} In addition, the noncrystalline anhydrate of magnesium acetate has been reported as the first example of a dehydration product that exhibits a glass transition phenomenon.⁹ Despite the fact that this process is a typical example of a glassy material formed through thermal decomposition, very limited studies have been conducted to reveal the kinetics and mechanism of the glass formation process. It has been reported that, in a quasi-sealed system, the thermal dehydration proceeds via an intermediate phase of melting.¹¹ In our preliminary experiment of the observation for the thermal dehydration process under an optical microscopy with a heating stage, existence of a fluid phase was clearly observed; see video clips in the Supporting Information. The previous studies and the preliminary microscopic observation indicate that, as a possible mechanism, glass formation in the thermal dehydration process

occurs via an intermediate fluid phase as in glass formation by the sol–gel process.

Magnesium acetate tetrahydrate is widely used as the precursor for the synthesis of magnesium oxide and magnesium containing oxides in the forms of thin film, rode, porous particles with high specific surface area, and so on,^{12–22} where ethanol-mediated sol–gel process and subsequent thermal decomposition of the as-prepared gel are the major chemical processes. For example, Bian et al.²⁰ reported a successful template-free synthesis of mesoporous magnesium oxide via the thermal decomposition of monodispersive crystalline particles of anhydrous magnesium acetate for the application in carbon dioxide adsorption. If the formation process of magnesium acetate anhydrous glass were mediated by an intermediate fluid phase, the glass material in varieties of size and morphology could be produced. In this case, magnesium acetate anhydrous glass can be the possible candidate for the precursor in such synthesis of magnesium ceramics, which realizes the potential applications. It is thus expected that elucidations of the kinetics and mechanism of the anhydrous glass formation via thermal dehydration and evaluation of the thermal stability of the as-produced anhydrous glass would contribute to the development

Received: May 30, 2012

Revised: November 18, 2012

Published: November 19, 2012

of a novel and efficient method of MgO synthesis by controlling the intermediate anhydrous glass phase and also provide a theoretical foundation for this kind of reactions in the solid state.^{23,24}

The present work was undertaken to reveal the kinetics and mechanism of the thermal dehydration of magnesium acetate tetrahydrate as an example of glass formation through a self-induced sol–gel process. The physicochemical events that take place during the reaction have been identified through consideration of complementary interpretations of the morphological changes of the reactant particles and the rate behavior of the mass-loss traces under different heating conditions. The formation of a hollow anhydrous glass is a novel finding of the study, and is discussed in detail in terms of the physicochemical mechanism and kinetics. In addition, the glass transition and in situ crystallization of the as-produced anhydrous glass are also characterized based on the morphological and kinetic studies. It is also expected that the present results provide fundamental information for the utilization of magnesium acetate anhydrous glass for applying as the precursor to the synthesis of magnesium ceramics.

2. EXPERIMENTAL SECTION

Reagent-grade magnesium acetate tetrahydrate (Sigma-Aldrich, Japan) was used as the starting material. After sieving to different fractions of particle size, the samples were characterized by powder X-ray diffraction (XRD, Rigaku RINT2200, monochrome Cu K α , 40 kV, 20 mA) and Fourier transform infrared spectroscopy (FT-IR, Shimadzu FT-IR 8400s, diffuse reflectance method, after diluting with KBr powder). The sample (ca. 10.0 mg) was weighed into a platinum cell (5 mm ϕ and 2.5 mm in height), and thermogravimetry–differential thermal analysis (TG-DTA, TGD-9600, ULVAC) was carried out at a heating rate $\beta = 5$ K min^{−1} in flowing N₂ (80 cm³ min^{−1}). The phase changes during stepwise heating of the selected samples were traced by powder XRD measurements using the above-described diffractometer equipped with a programmable heating chamber (PTC-20A, Rigaku). The sample particles were press-fitted on a platinum plate and heated at $\beta = 10$ K min^{−1} in flowing N₂ (100 cm³ min^{−1}). The diffraction measurements were carried out at various temperatures, with the sample temperature held constant for about 15 min during the measurements. The morphology of the samples heated to several selected temperatures during the above TG-DTA measurement was observed using a scanning electron microscope (SEM, JSM-6510, Jeol) after immediately cooling down to room temperature and coating with Pt by sputtering.

For the kinetic analysis of the thermal dehydration process, three different modes of temperature control were employed to record the mass-change traces: linear nonisothermal, isothermal, and controlled transformation rate modes. The mass-change traces under linearly increasing temperature at different β ($1.0 \leq \beta \leq 2.5$ K min^{−1}) were recorded using the above TG-DTA instrument (TGD-9600) under the identical conditions. Using a hanging-type TG instrument (TGA-50, Shimadzu), isothermal mass-change traces were recorded at different temperatures T ($325 \leq T \leq 341$ K) in flowing N₂ (80 cm³ min^{−1}) after heating the sample (10.0 mg weighed into a platinum cell: 6 mm ϕ and 2.5 mm in height) at $\beta = 10$ K min^{−1}. By equipping a homemade sample controlled thermal analysis (SCTA)²⁵ controller to the above TGA-50 instrument, the temperature profiles required for controlling the mass-loss

rate at different constant values C ($15 \leq C \leq 35$ $\mu\text{g min}^{-1}$) were recorded under conditions otherwise identical to those used for the isothermal measurements.

A batch of anhydrous magnesium acetate prepared by heating the sample (170–200 mesh) to 400 K at $\beta = 1$ K min^{−1} in flowing N₂ (100 cm³ min^{−1}) using a tube furnace was characterized as noncrystalline based on XRD analysis. The anhydrous sample (10.0 mg) was weighed into an aluminum cell (5 mm ϕ) and shielded with an aluminum lid by pressing. The shielded sample was subjected to differential scanning calorimetry (DSC, DSC-60, Shimadzu) measurements at different β ($1.0 \leq \beta \leq 10.0$ K min^{−1}) in flowing N₂ (50 cm³ min^{−1}).

3. RESULTS AND DISCUSSION

3.1. Overall Behavior of the Thermal Dehydration.

The sample was characterized as Mg(CH₃COO)₂·4H₂O by XRD and FT-IR; see Figures S1 and S2 in the Supporting Information. Figure 1a shows the TG-DTA curves for the

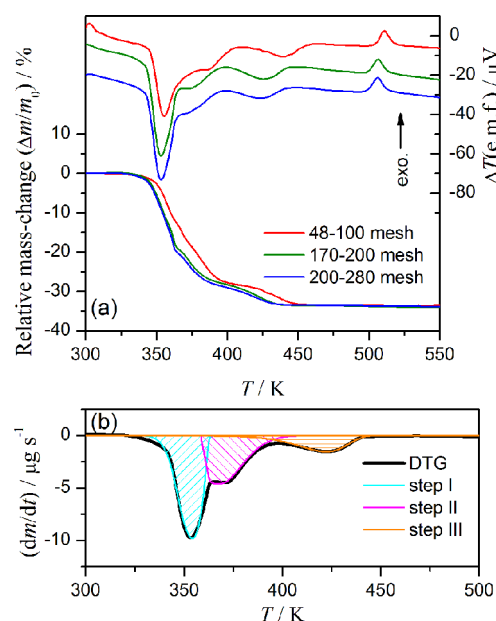


Figure 1. (a) TG-DTA curves for the thermal dehydration of Mg(CH₃COO)₂·4H₂O ($m_0 = 10.0$ mg) with different particle sizes at $\beta = 5$ K min^{−1} in flowing N₂ (80 cm³ min^{−1}) and (b) a typical example of the mathematical deconvolution of DTG curve for the sample (170–200 mesh) using the Weibull function.

samples with different particle sizes. The total mass-loss observed in the temperature range below 475 K was $33.60 \pm 0.08\%$, which closely corresponds to the stoichiometry of the reaction $\text{Mg}(\text{CH}_3\text{COO})_2 \cdot 4\text{H}_2\text{O} \rightarrow \text{Mg}(\text{CH}_3\text{COO})_2 + 4\text{H}_2\text{O}$. A complex thermal dehydration process is expected from the multistep mass-loss with the three distinguishable endothermic DTA peaks. From a rough estimation by mathematical deconvolution of the derivative TG (DTG) curves as is shown in Figure 1b for example, it was indicated that the extents of contribution of the respective mass-loss steps change systematically as a function of the particle size. The extent of contribution of the first mass-loss step increases systematically with decreasing particle size, which is accompanied by a decrease in that of the second mass-loss step. It should also be noted that an exothermic DTA peak is observed after

completion of the thermal dehydration. Figure 2 shows the TG-DTA curves for the thermal dehydration of the sample (170–

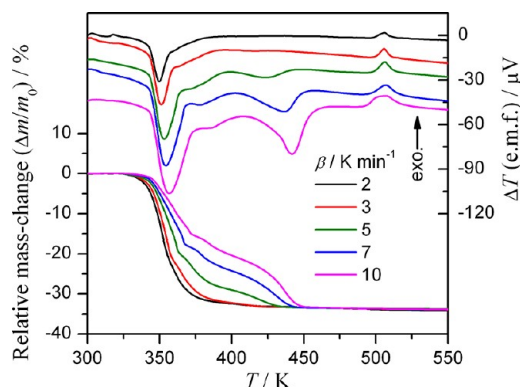


Figure 2. TG-DTA curves for the thermal decomposition of $\text{Mg}(\text{CH}_3\text{COO})_2 \cdot 4\text{H}_2\text{O}$ ($m_0 = 10.0$ mg, 170–200 mesh) at different β in flowing N_2 ($80 \text{ cm}^3 \text{ min}^{-1}$).

200 mesh) at different β in flowing N_2 . Changes in the extents of contribution of the respective mass-loss steps are also observed as a function of β . The systematic change in the extents of contribution of the three distinguished mass-loss steps with respect to β is characterized by an increase in that of the first mass-loss step with a decrease in β , accompanied by decreases in those of the second and third mass-loss steps. At lower β such as at 2 K min^{-1} , the mass-loss process takes place with a relatively smooth trace, in which the reaction completes at a temperature lower than the boiling point of water. The changes of the extents of contribution of the respective mass-loss steps with respect to particle size and β as roughly estimated by mathematical deconvolution using the Weibull function^{26–28} are listed in Table S1 in the Supporting Information.

Figure 3 shows the changes of the XRD patterns during heating the sample (170–200 mesh) in flowing N_2 . The XRD

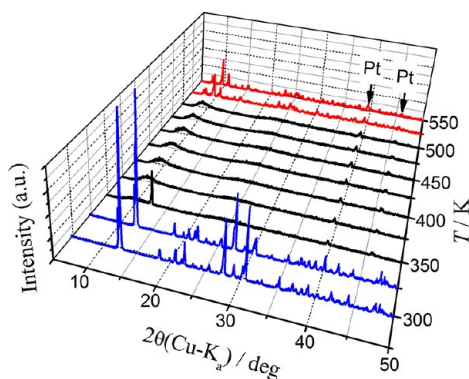


Figure 3. Changes in the XRD patterns of the sample (170–200 mesh) during stepwise heating in flowing N_2 ($100 \text{ cm}^3 \text{ min}^{-1}$).

peaks attributed to $\text{Mg}(\text{CH}_3\text{COO})_2 \cdot 4\text{H}_2\text{O}$ disappear at a very early stage of the thermal dehydration. During the course of the subsequent thermal dehydration, no distinguished crystalline phase is observed. The as-produced noncrystalline anhydrate transforms to crystalline anhydrous $\text{Mg}(\text{CH}_3\text{COO})_2$ at approximately 500 K, which corresponds to the exothermic DTA peak observed in Figures 1 and 2. The crystallization product is a mixture of two polymorphous phases of anhydrous

magnesium acetate; see Figure S3 in the Supporting Information. The FT-IR spectrum of the sample heated to 423 K does not indicate any absorption bands due to H_2O ; see Figure S4 in the Supporting Information. In addition, there is no distinguishable difference among the anhydrous magnesium acetates obtained by heating to 423, 473, and 523 K, irrespective of whether they are in the noncrystalline state at 423 and 473 K or crystalline state at 523 K. It is known that, in a closed system, the starting material used for these experiments melts at approximately 353 K.¹¹ The melting phenomenon is understood as the dissolution of $\text{Mg}(\text{CH}_3\text{COO})_2$ into the water evolved by the thermal dehydration of the tetrahydrate, thus forming a viscous fluid. In the present case of the thermal dehydration under a dynamic flow of inert gas, the evolved water or water vapor produced during the thermal dehydration is removed from the reaction system through diffusion and vaporization. On the basis of the disappearance of the XRD peaks of the tetrahydrate at an early stage of the thermal dehydration, premelting of the particle surface of the sample at an early stage of the thermal dehydration is very probable. In view of the optical microscopic observation provided as VC_MgAc002 in the Supporting Information, the initial reaction step is interpreted as the covering process of the surface by an intermediate fluid phase. In this case, the overall mass-loss behavior of the thermal dehydration is controlled not only by the chemical reaction at the reaction interface but also by the removal of water molecules from the surface fluid layer. Given that noncrystalline anhydrate is produced, the overall thermal dehydration process is similar to the sol–gel process in glass formation. Such a self-induced sol–gel process-like phenomenon has been reported for the thermal dehydration of alkaline earth borate hydrates^{3–6} and monohydrocalcite.^{7,8}

3.2. Morphological Changes during the Thermal Dehydration. Figure 4 illustrates the changes in the surface morphology of the sample particles (170–200 mesh) during the thermal dehydration at $\beta = 2 \text{ K min}^{-1}$ in flowing N_2 . The sample particles are initially columnar crystals (Figure 4a) with rough surfaces and surface cracks (Figure 4b). At the very early stage of thermal dehydration (Figure 4c; fractional reaction $\alpha = 0.06$), bright spots appear on the surface. The bright spots indicate swelling of the surface with a crack at the center (Figure 4d). The swelled surface indicates the formation of a fluid phase. The thermal dehydration likely proceeds in the fluid part on the surface, with the fluid portion radiating outward as reaction advances, as is the case for surface nucleation and subsequent growth.^{29–32} After exceeding $\alpha = 0.15$, large cracks radiating all over the surface are visible (Figure 4e; $\alpha = 0.18$). Crack formation over the entire surface indicates that the entire surface is covered with the fluid phase. This conclusion is also supported by the smooth surfaces of the sample particles at this stage in comparison with those of the reactant particles (Figure 4f). At the same time, small holes of $\sim 100 \text{ nm}$ can be seen on the surface, which are probably traces of diffusion channels for the evolution of water vapor. In parallel with the completion of covering the surfaces by the fluid phase, the volume of the fluid phase may expand in toward the center of the particles. In this situation, the destruction of the crystalline reactant is taking place at the interface between the fluid phase and the reactant crystal, while the uptake of water molecules from the reacting particles is being mediated by the surface fluid layer. Accordingly, the overall behavior of the thermal dehydration observed by the mass-loss measure-

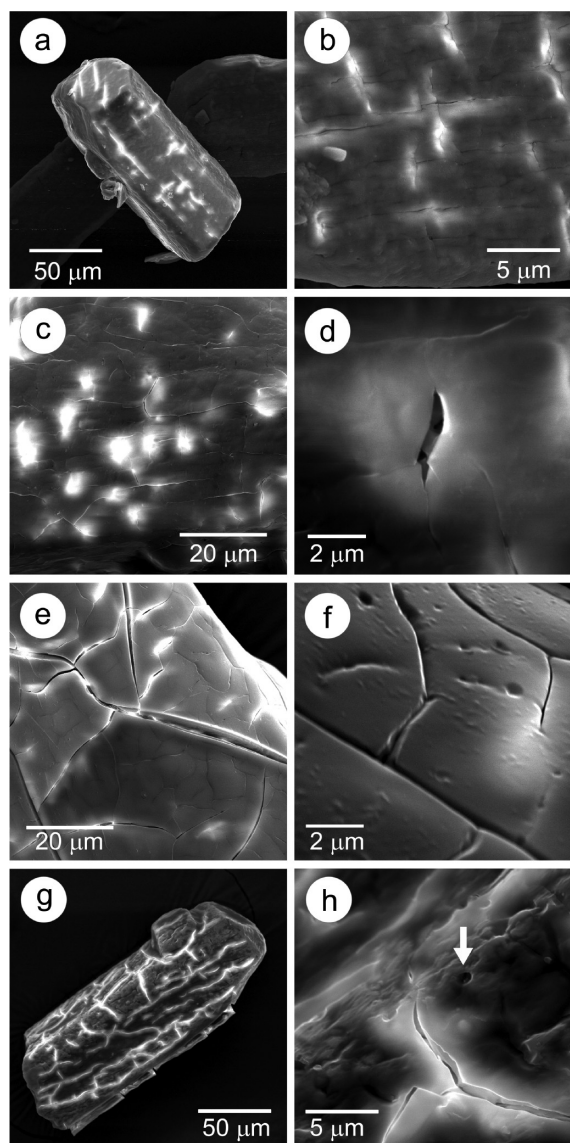


Figure 4. Typical SEM images of the sample (170–200 mesh) heated at $\beta = 2 \text{ K min}^{-1}$ to different temperatures in flowing N_2 ($80 \text{ cm}^3 \text{ min}^{-1}$): (a,b) reactant particle, (c,d) 333 K ($\alpha = 0.06$), (e,f) 343 K ($\alpha = 0.18$), and (g,h) 423 K ($\alpha = 1.00$) where the arrow indicates a hole.

ments is regulated largely by the nature of the surface fluid phase or layer, and the nature of this layer, particularly the fluidity, varies as the reaction advances and the quantity of water molecules and temperature change. The dehydration product maintains the external form of the columnar particle (Figure 4g), indicating that the fluidity of the surface fluid phase is not so high as to lead to the joining of neighboring particles. The surface of the dehydration product is rolling with large cracks irradiating over the entire surface and holes of several hundred nanometers (Figure 4h). The increased roughness of the product surface indicates that the fluidity of the layer decreases at the final stage of the thermal dehydration process due to the lower quantity of water molecules.

Changes in the surface morphology of sample particles during heating at a higher β ($=10 \text{ K min}^{-1}$) are shown in Figure 5. As was expected from the TG-DTA curves heated at a higher β , the changes in the surface textures during the course of the thermal dehydration are clearly different from those observed at a lower β . A significant difference is the appearance of dark

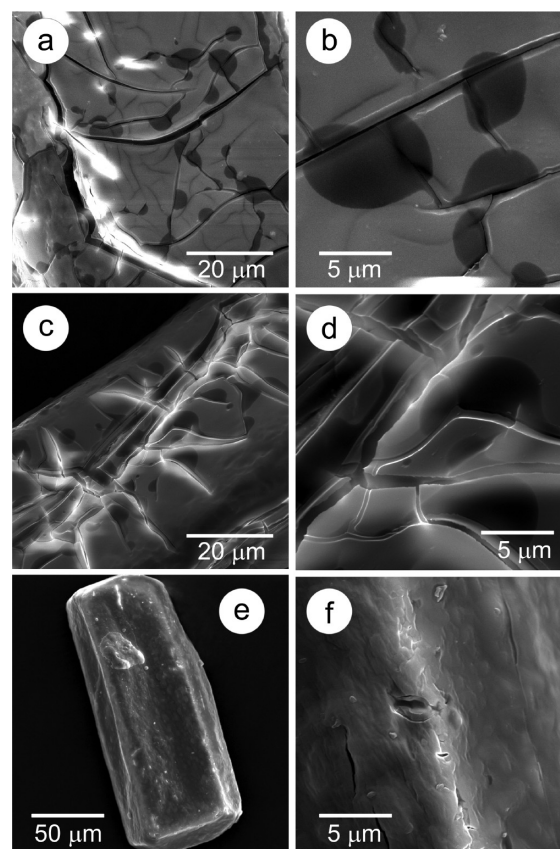


Figure 5. Typical SEM images of the sample (170–200 mesh) heated at $\beta = 10 \text{ K min}^{-1}$ to different temperatures in flowing N_2 ($80 \text{ cm}^3 \text{ min}^{-1}$): (a,b) 373 K ($\alpha = 0.36$), (c,d) 398 K ($\alpha = 0.79$), and (e,f) 473 K ($\alpha = 1.00$).

spots on the surface at the second mass-loss step (Figure 5a; $\alpha = 0.36$). The dark spots appear at the edge of cracks and correspond to hollow places of the surface fluid layer (Figure 5b). Because the peak top of the DTG curve of the second mass-loss step is close to 373 K, the hollow places are probably the traces of the rapid escape of water molecules from the surface fluid layer by evaporation. On heating further to the end of the second mass-loss step, the surfaces of the reacting particles undulate noticeably (Figure 5c; $\alpha = 0.79$), with large cracks and holes of several micrometers (Figure 5d). The drastic change in the surface texture indicates violent behavior of the water vapor escaping from the surface fluid layer. During the third mass-loss step, the surface texture once again changes drastically and becomes smooth (Figure 5e,f; $\alpha = 1.00$). It is assumed based on the formation of the smooth surface that the removal of water from the surface fluid layer during the third mass-loss step proceeds via a more moderate reaction compared to that of the second mass-loss step, and the surface layer retains a high enough fluidity to re-form.

The internal texture of the particles heated linearly to 473 K was observed after lightly crushing the samples. Irrespective of the different thermal dehydration pathways depending on the β , the as-produced particles were hollow. Figure 6 compares the SEM images of the internal surfaces of the hollow particles produced by heating at β of 2 and 10 K min^{-1} . The appearance of the internal surfaces of the hollow particles is complex in comparison with that of the outer surfaces, showing branches and bridges. Formation of the hollow structure indicates that the interior of the particle becomes fluid for a certain period

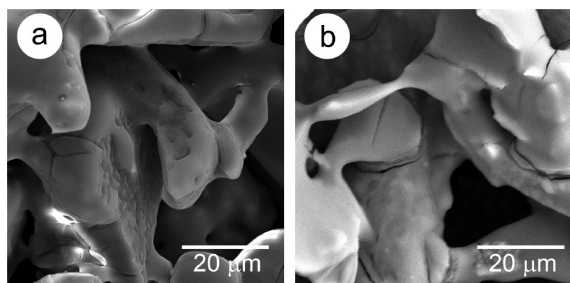


Figure 6. Typical SEM images of the internal texture of the sample (170–200 mesh) heated to 473 K in flowing N_2 ($80 \text{ cm}^3 \text{ min}^{-1}$) at (a) $\beta = 2 \text{ K min}^{-1}$ and (b) $\beta = 10 \text{ K min}^{-1}$.

during the course of the reaction. The evolved water vapor in the interior of the particles is trapped inside, because the diffusion to the outside of the particle is impeded by the surface layer. As the internal gaseous pressure increases, the partially dehydrated internal fluid phase becomes part of the surface, which further impedes the diffusion of the internal water vapor to the outside of the particle. The formation of the hollow center and the removal of the internal water vapor through the surface fluid layer by diffusion are likely the main processes occurring in the reaction, regardless of the different mass-loss behaviors at different β . The surface cracks observed in Figures 4 and 5 are possibly the channels for the diffusion of internal water vapor. The final stage seems to be the thermal dehydration of the outer shell of the hollow particle. Because the surface textures of the internal surfaces of the outer shells (Figure 6) are nearly identical with the outer surfaces of the respective particles heated at different β (Figures 4h and 5f), the final uptake of water molecules proceeds simultaneously at the outer and inner surfaces of the shell.

Under isothermal conditions at a temperature near the initiation temperature for thermal dehydration, the thermal dehydration proceeds at a moderate mass-loss rate. Figure 7

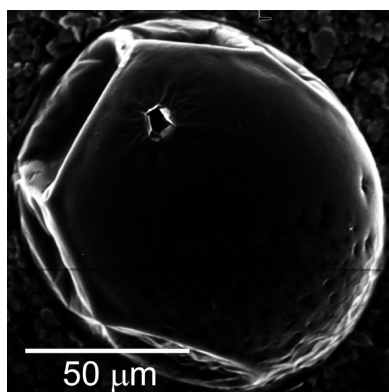


Figure 7. Typical SEM image of the dehydration product ($\alpha = 1.00$) obtained by heating the sample (170–200 mesh) isothermally at 325 K for 200 min in flowing N_2 ($80 \text{ cm}^3 \text{ min}^{-1}$).

shows a typical SEM image of the dehydration product, which is noncrystalline based on XRD analysis. The apparent swelling indicates the formation of hollow particles. Under such a moderate reaction rate, a higher internal pressure of water vapor is generated during the reaction because diffusion of internal water vapor is difficult due to a lack of possible channels or cracks in the surface fluid layer. At the same time, the fluidity of the surface layer seems to be relatively high due

to the higher content of water molecules. As a result, the product particles become hollow spheres due to swelling.

In contrast to the perfect melting of the reactant particles on heating in the quasi-closed system,¹¹ the fluid particle is retained during the course of reaction in the open system of dynamic flow of N_2 . This is likely due to relatively lower fluidity of the surface fluid layer by the continuous water uptake from the surface fluid layer.

3.3. Apparent Kinetics of the Thermal Dehydration. It has been observed above in Figure 2 that the thermal dehydration takes place with a smooth mass-loss behavior at a lower β ; that is, it occurs with a moderate mass-loss rate condition and at a temperature lower than the boiling point of water. Conventional isothermal mass-loss measurements and controlled rate thermal analysis (CRTA)²⁵ are suitable techniques for recording kinetic rate data under such a moderate mass-loss scenario. Figure 8 shows the isothermal

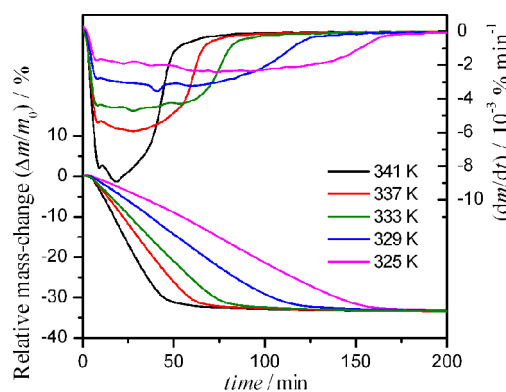


Figure 8. Isothermal mass-change traces and the corresponding derivative curves for the sample (170–200 mesh, $m_0 = 10.0 \text{ mg}$) at different temperatures in flowing N_2 ($80 \text{ cm}^3 \text{ min}^{-1}$).

mass-loss traces for the sample (170–200 mesh) at different temperatures in flowing N_2 . Smooth and nearly linear mass-loss traces were recorded at constant temperatures. A typical CRTA record at $C = 20.0 \mu\text{g min}^{-1}$ is shown in Figure 9a. The mass-loss rate was successfully regulated to remain constant during the course of thermal dehydration, and the temperature profile indicates a nearly constant temperature over the wide range of the reaction. Figure 9b shows the temperature profile during the course of the reaction at different C . With increasing C , the temperature profile shifts systematically to higher temperatures but maintains the same shape.

To evaluate the overall kinetics of the thermal dehydration, the kinetic rate data converted from the isothermal mass-loss traces and CRTA records were analyzed simultaneously by assuming the following differential kinetic equation^{33–37}

$$\frac{d\alpha}{dt} = A \exp\left(-\frac{E_a}{RT}\right) f(\alpha) \quad (1)$$

where α , A , and E_a are the fractional reaction, the Arrhenius preexponential factor, and the apparent activation energy, respectively. The kinetic model function $f(\alpha)$ expresses the physicochemistry of the reaction.^{38,39} Figure 10 illustrates the results of the formal kinetic analysis for the thermal dehydration of the sample (170–200 mesh). Taking the logarithms of eq 1, we obtain

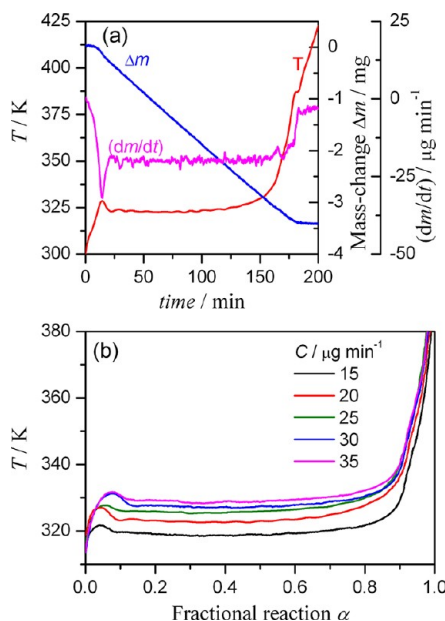


Figure 9. Results of the CRTA measurements for the thermal dehydration of the sample (170–200 mesh, $m_0 = 10.0$ mg) in flowing N_2 ($80 \text{ cm}^3 \text{ min}^{-1}$). (a) Typical record of CRTA measurement at $C = 20.0 \text{ } \mu\text{g min}^{-1}$ and (b) temperature profiles during the course of the reaction at different C .

$$\ln\left(\frac{d\alpha}{dt}\right) = \ln[Af(\alpha)] - \frac{E_a}{RT} \quad (2)$$

According to eq 2, the data points of the respective kinetic rate data at a selected α should create a straight line on the plot of $\ln(d\alpha/dt)$ against T^{-1} . The isoconversional plots, known as the Friedman plot,⁴⁰ at different α from 0.1 to 0.9 in steps of 0.1 are shown in Figure 10a. Regardless of the isothermal mass-loss traces and the CRTA measurements, the data points ($\ln(d\alpha/dt)$, T^{-1}) at the restricted α form a line. The slopes of the plots, $-E_a/R$, at the respective α are nearly constant in the range $0.1 \leq \alpha \leq 0.8$. The values of E_a evaluated from the slopes of the Friedman plots at different α are shown in Figure 10b. The fluctuation of E_a at the very beginning of the reaction corresponds to the surface reaction, as observed in Figure 4, c and d. The temperature drop at the beginning of the CRTA measurements is also evidence of surface nucleation and growth.^{7,41,42} The subsequent reaction in the range $0.08 \leq \alpha \leq 0.86$ is characterized by a constant value of $E_a = 76.4 \pm 1.0 \text{ kJ mol}^{-1}$, indicating that formation of the hollow center and diffusion of the internal water vapor through the surface fluid layer proceed at a steady rate. During the final stage of the mass-loss process, which corresponds to the reaction tails of the isothermal mass-loss traces and the temperature rise under the constant mass-loss rate, the E_a value declines rapidly reaching a minimum at $\alpha = 0.94$. It is thus concluded that the thermal dehydration from the as-produced outer shell takes place via a different mechanistic process than that of the established reaction, where the isoconversional relationship of eq 2 is not satisfied among the mass-loss data under the different heating conditions applied. Nearly the same trend for the E_a value, namely its α -dependence, was observed for the isothermal dehydration of samples of different particle sizes in flowing N_2 , where the value of E_a averaged over the different-sized samples was $72.2 \pm 3.1 \text{ kJ mol}^{-1}$ in the range $0.1 \leq \alpha \leq 0.8$.

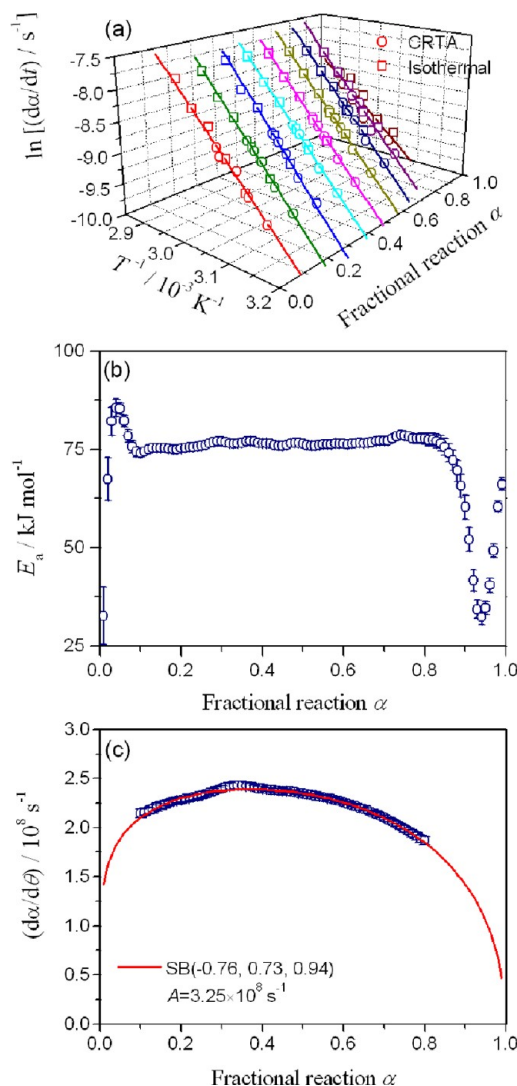


Figure 10. Kinetic results for the thermal dehydration of the sample (170–200 mesh, $m_0 = 10.0$ mg) under isothermal and controlled rate conditions in flowing N_2 ($80 \text{ cm}^3 \text{ min}^{-1}$). (a) Friedman plots at different α from 0.1 to 0.9 in steps of 0.1, (b) the values of E_a at different α , and (c) the experimental master plot and the fitted curves using the SB(m,n,p) model.

Within the α range where E_a is constant, that is, $0.1 \leq \alpha \leq 0.8$, an experimental master plot was drawn by extrapolating the rate data at the respective α to the infinite temperature according to^{33–36}

$$\frac{d\alpha}{d\theta} = \frac{d\alpha}{dt} \exp\left(\frac{E_a}{RT}\right), \quad \text{with } \theta = \int_0^t \exp\left(-\frac{E_a}{RT}\right) dt \quad (3)$$

where θ is Ozawa's generalized time^{43,44} and denotes the hypothetical reaction rate extrapolated to infinite temperature. The plot of $(d\alpha/d\theta)$ against α is the experimental master plot to be correlated to A and $f(\alpha)$ by^{33–36}

$$\frac{d\alpha}{d\theta} = Af(\alpha) \quad (4)$$

Figure 10c shows the experimental master plot of $(d\alpha/d\theta)$ against α . During the established reaction with a constant value of E_a , the reaction rate remains nearly constant, with slightly convex shape of the experimental master plot. The overall rate behavior of the entire course of the reaction cannot be

described by any single physico-geometric reaction model utilized conventionally for solid-state reactions. For the empirical fitting of the experimental master plot, an empirical kinetic model function known as the Sestak–Berggren model $SB(m,n,p)$,^{45,46} $f(\alpha) = \alpha^m(1 - \alpha)^n[-\ln(1 - \alpha)]^p$, was employed. The experimental master plot was fitted satisfactorily by $SB(-0.76 \pm 0.31, 0.73 \pm 0.12, 0.94 \pm 0.30)$ with $A = (3.24 \pm 0.06) \times 10^8 \text{ s}^{-1}$. Based on the fitted curve, it can be seen that the reaction rate increases rapidly at the initial stage of the reaction due to nucleation and growth on the surface. The nearly constant rate behavior of the experimental master plot during the main portion of the reaction reflects the linear mass loss at a constant temperature, and the constant temperature at a constant mass-loss rate observed experimentally; see Figures 8 and 9. The zero-order-like behavior is likely the result of the characteristics of the dehydration from the surface fluid layer. At the final stage of the reaction ($\alpha > 0.8$), it is believed that the reaction rate decelerates steeply due to the difficulty of removing the residual water molecules from the outer shell of the hollow sphere in order to form the noncrystalline solid product.

3.4. Kinetic Deconvolution of the Multistep Mass-Loss Process. To analyze the multistep mass-loss process under nonisothermal conditions at different β (see Figure 2), the rate data at the respective β were deconvoluted by assuming the following kinetic equation for the overall mass-loss process^{42,47–50}

$$\frac{d\alpha}{dt} = \sum_{i=1}^N c_i A_i \exp\left(-\frac{E_{a,i}}{RT}\right) f_i(\alpha_i),$$

with $\sum_{i=1}^N c_i = 1$ and $\sum_{i=1}^N c_i \alpha_i = \alpha$ (5)

where the overall reaction rate is expressed by the summation of the reaction rate of the different mass-loss steps, i , by considering the extent of contribution of the different mass-loss steps, c_i . By utilizing $SB(m,n,p)$ as the kinetic model functions of the different mass-loss steps, $f_i(\alpha_i)$, the most appropriate parameters of c_i , A_i , $E_{a,i}$, m_i , n_i , and p_i for the different mass-loss steps were optimized simultaneously using a nonlinear least-squares analysis for minimizing the square sum of the residue when fitting the calculated curve of $(d\alpha/dt)_{\text{cal}}$ versus time to the experimental curve of $(d\alpha/dt)_{\text{exp}}$ versus time.^{43,47–50}

$$F = \sum_{j=1}^M \left[\left(\frac{d\alpha}{dt} \right)_{\text{exp},j} - \left(\frac{d\alpha}{dt} \right)_{\text{cal},j} \right]^2$$

(6)

Figure 11 shows the typical results of the kinetic deconvolution for the thermal dehydration of the sample (170–200 mesh) at $\beta = 5 \text{ K min}^{-1}$. The rate data at the different β were deconvoluted successfully into three mass-loss steps, with the R^2 values of the nonlinear least-squares analysis better than 0.99. Although the present kinetic deconvolution is just a possible method of kinetic simulation to obtain a further insight into the overlapped process, the resolved kinetic curve indicates the agreeable features. For example, in the second reaction step, bubbling is observed in the optical microscopic observation provided as VC_MgAc002 in the Supporting Information. In the same temperature region, the resolved kinetic curve for the first mass-loss step indicates a shoulder. This behavior is interpreted as the enhancement of the first mass-loss process of the dehydration from the surface fluid

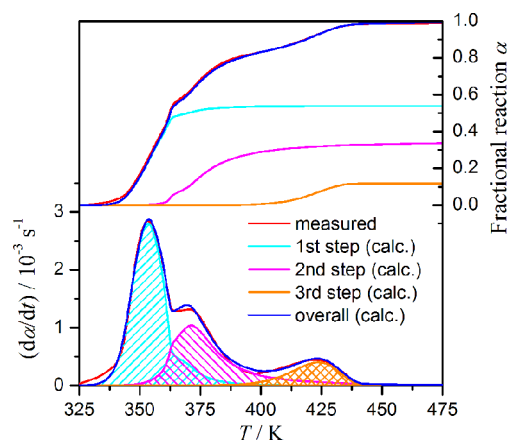


Figure 11. Typical results of the kinetic deconvolution for the thermal decomposition of the sample (170–200 mesh, $m_0 = 10.0 \text{ mg}$) at $\beta = 5 \text{ K min}^{-1}$ in flowing N_2 ($80 \text{ cm}^3 \text{ min}^{-1}$).

Table 1. Changes of the Extent of Contribution of the Different Mass-Loss Steps in the Thermal Dehydration of $\text{Mg}(\text{CH}_3\text{COO})_2 \cdot 4\text{H}_2\text{O}$ (170–200 mesh, $m_0 = 10.0 \text{ mg}$) in Flowing N_2 ($80 \text{ cm}^3 \text{ min}^{-1}$) as a Function of β

$\beta/\text{K min}^{-1}$	R^2	extent of contribution/%		
		step I	step II	step III
2	0.9973	89.73	5.75	4.52
3	0.9960	73.78	22.81	3.40
5	0.9980	53.80	34.43	11.77
7	0.9986	47.77	27.43	24.81
10	0.9912	46.27	18.07	35.65

layer by the violent dehydration action of the second mass-loss step. Table 1 lists the optimized values of the extent of contribution, c_i , of the three mass-loss steps at the respective β . The same trend of the β -dependent variations of c_i as estimated roughly by the mathematical deconvolution using the Weibull function (see Table S1 in the Supporting Information) is observed. The extent of contribution of the first mass-loss step decreases with increasing β , which is compensated by the systematic increase in that of the third mass-loss step. The extent of contribution of the second mass-loss step reaches a maximum at $\beta = 5 \text{ K min}^{-1}$. Regardless of the β -dependent change in those c_i values, the apparent kinetic parameters for the different mass-loss steps evaluated for the reaction at different β remain practically constant values. Table 2 lists the average kinetic parameters for the respective reaction steps in the reactions at different β . The apparent value of E_a for the first reaction step is practically identical to that evaluated for the thermal dehydration under isothermal and controlled rate conditions. It should be noted in Figure 11 that the maximum rate of the second mass-loss step is observed at near the boiling point of water, which indicates the vaporization of water from the surface fluid layer of the reacting particle. The process is described by a slightly smaller value of $E_a = 62.4 \pm 0.3 \text{ kJ mol}^{-1}$ compared with that for the thermal dehydration at temperatures below the boiling point of water. The third mass-loss step is characterized by a value of $E_a = 81.1 \pm 3.0 \text{ kJ mol}^{-1}$, which is slightly larger in comparison with that for the first mass-loss step. In spite of the change in the extent of contribution of the different mass-loss steps as a function of β , the kinetic exponents evaluated for the respective reaction steps are also nearly identical. All of the empirical $SB(m,n,p)$ models

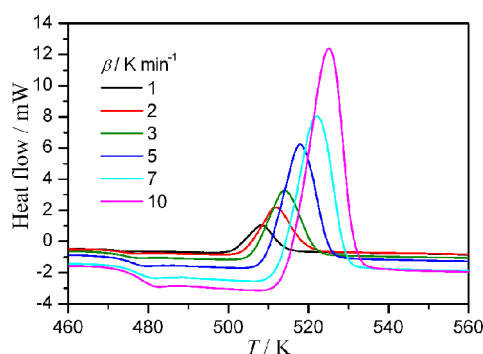
Table 2. Kinetic Parameters for the Respective Mass-Loss Steps in the Nonisothermal Dehydration of $\text{Mg}(\text{CH}_3\text{COO})_2 \cdot 4\text{H}_2\text{O}$ (170–200 mesh, $m_0 = 10.0$ mg) in Flowing N_2 ($80 \text{ cm}^3 \text{ min}^{-1}$) Averaged for the Results at Different β

mass-loss step	$E_a/\text{kJ mol}^{-1}$	A/s^{-1}	kinetic exponents		
			m	n	p
first	74.3 ± 0.2	$(1.56 \pm 0.79) \times 10^9$	0.67 ± 0.04	1.86 ± 0.35	-0.01 ± 0.01
second	62.4 ± 0.3	$(1.15 \pm 0.04) \times 10^7$	-0.01 ± 0.01	3.28 ± 0.22	0.79 ± 0.09
third	81.1 ± 3.0	$(4.83 \pm 0.16) \times 10^7$	0.45 ± 0.33	0.84 ± 0.12	-0.16 ± 0.42

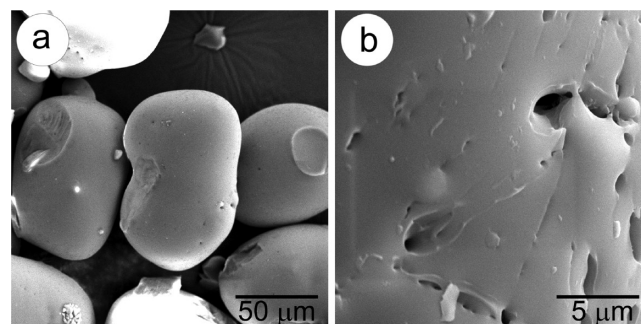
evaluated for the different reaction steps indicate a maximum on the way of the reaction (see Figure S5 in the Supporting Information). The decelerating portions of the first and second mass-loss steps are concave in shape, indicating diffusion-controlled behavior. In contrast, the overall behavior of the third mass-loss step is well fitted by a Johnson–Mehl–Avrami type model for nucleation and subsequent growth,^{38,39} $\text{JMA}(m) = m(1 - \alpha)[- \ln(1 - \alpha)]^{1-1/m}$, with $m = 1.39 \pm 0.01$.

Combined with the changes in the surface texture of the sample particles during the thermal dehydration observed in Figures 4–7, the changes in the mass-loss behavior of multistep processes and the extents of contribution of the different mass-loss steps depending on heating conditions and particle size are interpreted in relation to the change in the condition of the fluid phase, that is, the water content and fluidity, and to the mechanism of escape of the water molecules from the fluid phase. The second mass-loss step appears when the thermal dehydration takes place above the boiling point of water. The violent action of the water molecules escaping by boiling and bubbling from the water-rich surface fluid layer and internal fluid phase is expected based on the overall kinetic behavior of the second mass-loss step and the surface texture of the sample particles at this stage, see the video clip VC_MgAc002 in the Supporting Information. The third mass-loss step is the result of water escaping from the outer shell of the hollow particles with a reduced water content, where the fluidity of the phase is still maintained due to the higher temperature. In this stage, the glass network seems to be nearly constructed. The thermal dehydration proceeds as a function of the water uptake process of the reacting particle within the glass network with an overall rate behavior associated with the growth of nuclei controlled by diffusion.

3.5. Kinetics of the in Situ Crystallization. Figure 12 shows the DSC curves for the product of the thermal dehydration at different β . As unambiguous evidence for glass formation through thermal dehydration, a glass transition

**Figure 12.** DSC curves for the crystallization of anhydrous magnesium acetate at different β , produced by the thermal dehydration of the tetrahydrate (170–200 mesh) at $\beta = 1 \text{ K min}^{-1}$ in flowing N_2 ($100 \text{ cm}^3 \text{ min}^{-1}$).

behavior is observed at approximately 470 K as an endothermic anomaly in the DSC curves. The dependence of the glass transition temperature on β and the Kissinger-type plot⁵¹ for the glass transition are shown in Figure S6 in the Supporting Information. Although the application of the Kissinger-type equation to the relaxation phenomena is rough approximation, the value of E_a for the relaxation process was determined to be $E_a = 556.4 \pm 16.7 \text{ kJ mol}^{-1}$, which is in good agreement with that reported in the first study of the glass transition phenomenon of the dehydration product.⁹ Crystallization of anhydrous magnesium acetate takes place with a well-shaped DSC exotherm. From the peak area of the DSC curves, the average enthalpy change of crystallization for the reactions at different β was determined to be $\Delta H = -13.3 \pm 0.8 \text{ kJ (mol Mg}(\text{CH}_3\text{COO})_2)^{-1}$. Typical SEM images of the particles after crystallization are shown in Figure 13. The morphology of the

**Figure 13.** Typical SEM images of the sample (170–200 mesh) heated linearly to 523 K at $\beta = 2 \text{ K min}^{-1}$ in flowing N_2 ($80 \text{ cm}^3 \text{ min}^{-1}$).

reacting particles changes drastically during the course of crystallization to form a cocoon-like appearance (Figure 13a). The volume shrinkage of the particles is apparent by comparing them with the particles of anhydrous glass (see Figures 4g and 5e). Craterlike depressions observed on the surface of the crystallized particles are likely the traces of contact with neighboring particles, indicating a high fluidity of the reacting particles during the course of crystallization. The formation process of the craterlike depression can be clearly seen in the video clip VC_MgAc003 in the Supporting Information. Large numbers of holes are also observed on the surface of the crystallized particles (Figure 13b). These holes are the traces of the cracks in the outer shell produced during the thermal dehydration and of the hollow structure of the as-produced anhydrous glass. These are to be the diffusion channel of gases enclosed in the hollow structure of the anhydrous glass during the volume shrinkage by crystallization (see VC_MgAc003 in the Supporting Information). From these observations, it is concluded that the crystallization process of as-produced anhydrous glass is accompanied by long distance movement of chemical species in a matrix that has an appreciable fluidity.

Figure 14 shows the results of the kinetic calculation for the DSC exothermic peaks of crystallization at different β . Although

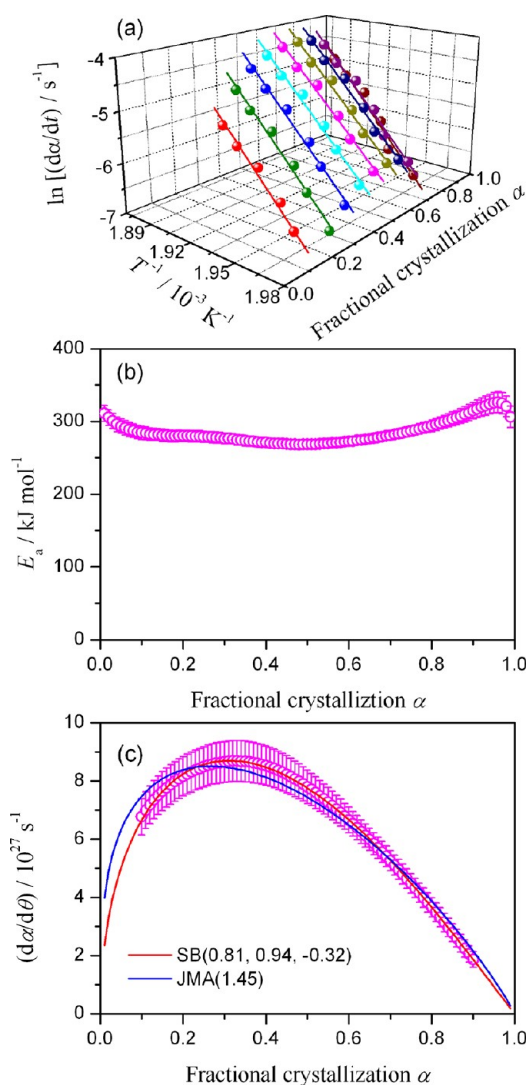


Figure 14. Kinetic results of the crystallization of as-produced anhydrous magnesium acetate. (a) Friedman plots at different α from 0.1 to 0.9 in steps of 0.1, (b) the values of E_a at different α , and (c) the experimental master plot and the fitting curves using the SB(m,n,p) and JMA(m) models.

the Friedman plots indicate acceptable straight lines irrespective of α (Figure 14a), the apparent values of E_a calculated from the Friedman plots increase slightly in the second half of the process $\alpha > 0.6$ (Figure 14b). The observed volume shrinkage of the particle seems to be related to the apparent change in the values of E_a during the second half of the crystallization process. Using the value $E_a = 280.1 \pm 9.8 \text{ kJ mol}^{-1}$, which is averaged over $0.1 \leq \alpha \leq 0.9$, an experimental master plot was drawn according to eq 3 (see Figure 14c). The experimental master plot is fitted nearly perfectly by SB($0.81 \pm 0.13, 0.94 \pm 0.05, -0.32 \pm 0.13$), with $A = (2.34 \pm 0.03) \times 10^{28} \text{ s}^{-1}$. Applying JMA(m), the value of $m = 1.45 \pm 0.01$ was optimized with $A = (1.67 \pm 0.01) \times 10^{28} \text{ s}^{-1}$. The fitting using JMA(1.45) is inferior to that using SB(0.82, 0.94, -0.32), but the kinetic exponent $m = 1.45$ can be interpreted as indicating the three-dimensional growth of nuclei controlled by diffusion of chemical species. The structural characteristics are, therefore,

predicted by the comparable kinetic models evaluated for the final stage of the thermal dehydration and for the in situ crystallization of as-produced anhydrous glass. Further detailed characterization on the nature of the as-produced anhydrous glass and its variation depending on the formation conditions are necessary to reveal the formation mechanism of crystalline polymorphs of anhydride and the crystallization kinetics. The works are left for future works.

4. CONCLUSIONS

The thermal dehydration of magnesium acetate tetrahydrate is initiated on the surface of reacting particles by the formation of a fluid phase produced by melting and/or dissolution of ionic species into the produced water. The reaction accelerates as the area of fluid phase expands on the surface, and the evolution of water vapor takes place from the surface of the fluid phase. After the original surface is covered by the fluid phase, the reaction moves to the established reaction stage, which is characterized by the advancement of the interface of the fluid layer and the original crystal of the tetrahydrate. The zero-order-like reaction behavior with $E_a \approx 70\text{--}80 \text{ kJ mol}^{-1}$ under isothermal conditions in the temperature range below 350 K indicates that the mass-loss behavior is regulated by the evaporation of water on the surface of the fluid layer. Because the diffusion of water through the surface fluid layer is restricted, the internal water vapor pressure increases as reaction advances. This pressure leads to formation of a hollow structure as a result of movement of the internal fluid phase to the direction of the surface layer. Under dynamic heating at a higher heating rate, the reaction temperature range of the thermal dehydration is beyond 373 K. The violent dehydration behavior of the boiling/evaporation of water in the fluid phase is observed as the second mass-loss step. The formations of cracks and holes on the surface are the traces of this violent dehydration action. The final stage of the reaction is the dehydration from the shell of the as-produced hollow particle. Under moderate reaction conditions below 350 K, spherical hollow particles are produced by swelling due to the limited diffusion channels for the internal water vapor. The final stage of the thermal dehydration is characterized, with $E_a \approx 80 \text{ kJ mol}^{-1}$, by the three-dimensional growth of the anhydrate controlled by diffusion. The as-produced hollow particles are in the glass state, with the glass transition at approximately 470 K. The crystallization of the anhydrous glass takes place before the thermal decomposition of anhydrate with $\Delta H = -13.3 \text{ kJ mol}^{-1}$. The mechanism of the crystallization resembles that for the final stage of the thermal dehydration, that is, the three-dimensional growth controlled by diffusion, with $E_a \approx 280 \text{ kJ mol}^{-1}$. Smaller and rounded particles are obtained as the crystallization product of the anhydrate.

■ ASSOCIATED CONTENT

Supporting Information

Powder XRD pattern and FT-IR spectrum of the starting material. Extents of contribution of the respective mass-loss steps of the multistep thermal dehydration roughly evaluated by mathematical deconvolution. XRD patterns and FT-IR spectra of dehydrated and crystallized products. Experimental master plots for the respective mass-loss steps of the multistep thermal dehydration. Kinetic behavior of the glass transition phenomenon of the as-produced magnesium acetate anhydrous glass. Video clips of optical microscopic observations of the course of the thermal dehydration and in situ crystallization. This

material is available free of charge via the Internet at <http://pubs.acs.org>.

AUTHOR INFORMATION

Corresponding Author

*Tel./Fax: +81-82-424-7092. E-mail: nkoga@hiroshima-u.ac.jp.

Notes

The authors declare no competing financial interest.

ACKNOWLEDGMENTS

The present work was partially supported by a grant-in-aid for scientific research (B) (21360340 and 22300272) from Japan Society for the Promotion of Science.

REFERENCES

- (1) Galwey, A. K. *Thermochim. Acta* **2000**, 355, 181–238.
- (2) Koga, N.; Tanaka, H. *Thermochim. Acta* **2002**, 388, 41–61.
- (3) Koga, N.; Sestak, J. *J. Am. Ceram. Soc.* **2000**, 83, 1753–1760.
- (4) Koga, N.; Criado, J. M.; Tanaka, H. *J. Therm. Anal. Calorim.* **2002**, 67, 153–161.
- (5) Koga, N.; Tanaka, H. *J. Therm. Anal. Calorim.* **2005**, 82, 725–729.
- (6) Koga, N.; Utsuoka, T. *Thermochim. Acta* **2006**, 443, 197–205.
- (7) Kimura, T.; Koga, N. *J. Phys. Chem. A* **2011**, 115, 10491–10501.
- (8) Kimura, T.; Koga, N. *Cryst. Growth Des.* **2011**, 11, 3877–3884.
- (9) Onodera, N.; Suga, H.; Seki, S. *Bull. Chem. Soc. Jpn.* **1968**, 41, 2222.
- (10) McAdie, H. G.; Jervis, J. M. *Thermochim. Acta* **1970**, 1, 19–28.
- (11) Isa, K.; Nogawa, M. *Thermochim. Acta* **1984**, 75, 197–206.
- (12) Kumta, P. N.; Hackenberg, R. E.; McMichael, P.; Johnson, W. C. *Mater. Lett.* **1994**, 20, 355–362.
- (13) Chhor, K.; Bocquet, J. F.; Pommier, C. *Mater. Chem. Phys.* **1995**, 40, 63–68.
- (14) Kordas, G. J. *Mater. Chem.* **2000**, 10, 1157–1160.
- (15) Parola, S.; Khem, R.; Cornu, D. *J. Sol-Gel Sci. Technol.* **2003**, 26, 1109–1112.
- (16) Afonina, G. A.; Leonov, V. G.; Popova, O. N. *Glass Ceram.* **2005**, 62, 248–252.
- (17) Andrianov, N. T.; Abdel-gavad, S. R.; Zenkova, N. V. *Glass Ceram.* **2006**, 63, 415–418.
- (18) Afonina, G. A.; Leonov, V. G.; Popova, O. N. *Glass Ceram.* **2008**, 65, 447–451.
- (19) Shina, D.-Y.; Kim, K.-N. *J. Ceram. Proc. Res.* **2009**, 10, 536–540.
- (20) Bian, S.-W.; Baltrusaitis, J.; Galhotra, P.; Grassian, V. H. *J. Mater. Chem.* **2010**, 20, 8705.
- (21) Choi, H.; Hwang, S. J. *Mater. Res.* **2011**, 15, 842–845.
- (22) Zulkefle, H.; Ismail, L. N.; Bakar, R. A.; Mamat, M. H.; Rusop, M. *Int. J. Appl. Phys. Math.* **2012**, 2, 38–43.
- (23) Koga, N.; Maruta, S.; Kimura, T.; Yamada, S. *J. Phys. Chem. A* **2011**, 115, 14417–14429.
- (24) Pijolat, M.; Favregeon, L.; Soustelle, M. *Thermochim. Acta* **2011**, 525, 93–102.
- (25) Sorensen, O. T.; Rouquerol, J., Eds., *Sample Controlled Thermal Analysis*; Kluwer: Dordrecht, The Netherlands, 2003.
- (26) Cai, J.; Liu, R. *J. Phys. Chem. B* **2007**, 111, 10681–10686.
- (27) Janković, B.; Adnadić, B.; Kolar-Anić, L.; Smičiklas, I. *Thermochim. Acta* **2010**, 505, 98–105.
- (28) Perejon, A.; Sanchez-Jimenez, P. E.; Criado, J. M.; Perez-Maqueda, L. A. *J. Phys. Chem. B* **2011**, 115, 1780–1791.
- (29) Jacobs, P. W. M. *J. Phys. Chem. B* **1997**, 101, 10086–10093.
- (30) Favregeon, L.; Pijolat, M.; Valdivieso, F.; Helbert, C. *Phys. Chem. Chem. Phys.* **2005**, 7, 3723–3727.
- (31) Favregeon, L.; Pijolat, M.; Helbert, C. *J. Mater. Sci.* **2008**, 43, 4675–4683.
- (32) Favregeon, L.; Pijolat, M. *Thermochim. Acta* **2011**, 521, 155–160.
- (33) Ozawa, T. *J. Therm. Anal.* **1986**, 31, 547–551.
- (34) Málek, J. *Thermochim. Acta* **1992**, 200, 257–269.
- (35) Koga, N. *Thermochim. Acta* **1995**, 258, 145–159.
- (36) Gotor, F. J.; Criado, J. M.; Malek, J.; Koga, N. *J. Phys. Chem. A* **2000**, 104, 10777–10782.
- (37) Perez-Maqueda, L. A.; Criado, J. M.; Sanchez-Jimenez, P. E. *J. Phys. Chem. A* **2006**, 110, 12456–12462.
- (38) Tanaka, H.; Koga, N.; Galwey, A. K. *J. Chem. Educ.* **1995**, 72, 251–256.
- (39) Khawam, A.; Flanagan, D. R. *J. Phys. Chem. B* **2006**, 110, 17315–17328.
- (40) Friedman, H. L. *J. Polym. Sci. C* **1964**, 6, 183–195.
- (41) Koga, N.; Kimizu, T. *J. Am. Ceram. Soc.* **2008**, 91, 4052–4058.
- (42) Sanchez Jimenez, P. E.; Pérez-Maqueda, L. A.; Perejon, A.; Criado, J. M. *J. Phys. Chem. C* **2012**, 116, 11797–11807.
- (43) Ozawa, T. *Bull. Chem. Soc. Jpn.* **1965**, 38, 1881–1886.
- (44) Ozawa, T. *Thermochim. Acta* **1986**, 100, 109–118.
- (45) Sestak, J.; Berggren, G. *Thermochim. Acta* **1971**, 3, 1–12.
- (46) Šesták, J. *J. Therm. Anal.* **1990**, 36, 1997–2007.
- (47) Ferriol, M.; Gentilhomme, A.; Cochez, M.; Oget, N.; Mieloszynski, J. L. *Polym. Degrad. Stab.* **2003**, 79, 271–281.
- (48) Lopez, G.; Aguado, R.; Olazar, M.; Arabiourrutia, M.; Bilbao, J. *Waste Manag.* **2009**, 29, 2649–2655.
- (49) Sánchez-Jiménez, P. E.; Perejón, A.; Criado, J. M.; Diáñez, M. J.; Pérez-Maqueda, L. A. *Polymer* **2010**, 51, 3998–4007.
- (50) Koga, N.; Goshi, Y.; Yamada, S.; Perez-Maqueda, L. A. *J. Therm. Anal. Calorim.* **2012**, doi: 10.1007/s10973-012-2500-6.
- (51) Kissinger, H. E. *Anal. Chem.* **1957**, 29, 1702–1706.